

# An adhesion test method for spray-applied fire-resistive materials

Kar Tean Tan, Christopher C. White<sup>\*,†</sup> and Donald L. Hunston

*Building and Fire Research Laboratory, National Institute of Standards and Technology, Material and Construction Research Division, 100 Bureau Drive, Mail Stop 8615, Gaithersburg, MD 20899-8615, U.S.A.*

## SUMMARY

Adhesion of spray-applied fire-resistive materials (SFRMs) to steel structures is critical in enabling a building to remain functional during a fire for a specific period of time for life safety and fire department access. Empirical tests such as ASTM E736 have been widely adopted by the industry in an effort to ensure sufficient bonding between SFRMs and steel structures. ASTM E736 assesses the adhesion of SFRMs by using tensile strength, a failure parameter that depends on the test geometry and has limited use for predicting failure in other geometries and conditions. These limitations have produced an urgent need for a scientifically based adhesion test method. In this paper, we propose a new test method that would provide more fundamental information that is independent of test geometry and has predictive capability. This paper utilizes a fracture energy-based failure criterion ( $G_C$ ) to characterize the adhesion between SFRMs and steel. The theoretical basis of this test method is validated by experimental compliance tests. The dependence of  $G_C$  on various test variables such as specimen width, substrate type, SFRM formulation, and test rate are examined. A comparison between this new test method, and the current widely used strength-based test method is also presented. Copyright © 2010 John Wiley & Sons, Ltd.

Received 16 February 2010; Revised 31 March 2010; Accepted 5 April 2010

**KEY WORDS:** ASTM E736; adhesion; cantilever beam; fracture mechanics; spray-applied fire-resistive materials

## 1. INTRODUCTION

In the event of a fire, unprotected steel structures can be extremely vulnerable because the steel can soften, causing the structure to collapse. To mitigate this hazard, the steel is often coated with spray-applied fire-resistive materials (SFRMs) to limit its temperature rise during a fire event [1–5]. Various types of SFRMs are available in the marketplace; the main classes of materials include cementitious, fibrous, and composite products. Typically, SFRMs are designed to protect steel structures via their low thermal conduction properties, energy-absorbing reactions, and/or high effective heat capacity, etc. [1, 5]. All these protective mechanisms require stable adhesion between the SFRM and steel structures to function properly [6].

The standard adhesion test currently used in building codes is carried out according to the ASTM E736 [7]. This method involves bonding a metal or plastic disk containing an attached hook to the surface of the SFRM using a quick-setting adhesive, and attaching a spring-type weighing scale to the hook. The scale is pulled, and the bond strength is deemed acceptable if the SFRM is able to withstand a prescribed minimum force. While this test method is well known for its simplicity and ease of use, various criticisms have been raised. The most prominent limitation is

<sup>\*</sup>Correspondence to: Christopher C. White, Building and Fire Research Laboratory, National Institute of Standards and Technology, Material and Construction Research Division, 100 Bureau Drive, Mail Stop 8615, Gaithersburg, MD 20899-8615, U.S.A.

<sup>†</sup>E-mail: christopher.white@nist.gov

that this test method is strength-based, and relies solely on the measurements of ultimate tensile strength as the adhesion metric. Strength is a test condition-dependent parameter which generally provides little information on what may happen in other geometries or conditions. Thus, it does not help in developing an understanding of realistic structural behavior in a fire. More importantly, inherent flaws in materials are not realistically accounted in this approach. For brittle materials such as SFRMs, failure is generally initiated by a crack growth from flaws or defects that may be created in the application of the SFRM. These flaws are not reproducible and lead to large scatter in experimental data in strength-based tests. Measurements are often complicated by the need for a proper alignment of the bonded specimen and the applied force. It might be noted that the ASTM E736 requires the SFRM surface to be cut prior to conducting the test to limit the area involved in the measurement. This pre-cutting may prevent large debonded areas from contributing to the bond strength, hence more accurate values could be obtained. The cutting must be done carefully, however, since it can introduce flaws which would adversely affect the results, and this may not be easy to detect. Furthermore, there is no isolation of the adhesively bonded disk (diameter of 51–83 mm) from the pre-cut SFRM (surface areas of 300 mm  $\times$  300 mm and at least 100 mm  $\times$  300 mm for laboratory and field tests, respectively) so the amount of material debonded can vary from one test to the next. Thus, an alternate method based on sound scientific principles is highly desirable.

Recent building disasters attributed to a failure in the SFRM applied to structural steel have raised awareness of the shortcomings in the current standard test method, and have prompted the building community to seek improvements in the testing of SFRM adhesion [8–10]. The research reported here responds to this need by developing scientific test methods for measuring adhesion between SFRM and steel. Both a laboratory test and a field test are needed, and there are obvious advantages to filling both requirements with a single method. On the other hand, there are far greater limits on what can be done in the field environment, and the objectives for the two cases are different. In the field, the major goal for the test is quality control and verification of proper installation. With the laboratory test, the goals may include materials development, design information, basic understanding for what factors influencing adhesion. Consequently, it was decided in this program to develop both a laboratory test with maximum flexibility and a field test with a scientific basis. The purpose of this paper is to discuss the laboratory test, whereas the field test will be presented in a separate publication.

We adopted a fracture mechanics approach using an energy-based failure criterion with assumptions of linear elasticity and pre-existing flaws. Both assumptions are reasonable for SFRMs. This test quantifies critical strain energy release rate or fracture energy, which is a measure of the energy required to increase a crack by unit length in a specimen of unit width. As a linear elastic behavior is assumed, the fracture energy can be transformed into to a stress intensity factor if a stress-based failure criterion is desired. A single-arm cantilever beam (SACB) specimen geometry was selected as the configuration for these tests. This paper will demonstrate the advantages of this approach in producing a geometric-independent failure property that can quantitatively characterize the adhesion between SFRMs and steel. We anticipate that this test method will not only provide a scientific test protocol for evaluating and predicting the adhesion performance of materials, but also will help in defining the performance requirements that are needed for fire protection of steel structures in residential and commercial buildings.

## 2. MATERIALS AND METHODS<sup>‡</sup>

### 2.1. Materials

To evaluate the proposed test method, five commercial SFRMs encompassing the range of chemistries and formulations currently available in the marketplace were utilized. They were

<sup>‡</sup>Certain commercial products or equipments are described in this paper to specify adequately the experimental procedure. In neither case does such identification imply recommendation or endorsement by the National Institute of Standards and Technology, nor does it imply that it is necessary the best available for the purpose.

Table I. Various types of evaluated SFRMs.

Type of SFRM	
A	A low density, gypsum-based SFRM
B	A compositely reinforced fibrous SFRM
C	A medium density, portland cement-based SFRM
D	A high density, portland cement-based SFRM
E	A low density, gypsum-based SFRM

obtained from three of the primary manufacturers of SFRMs and are arbitrarily identified in this paper by the letters A through E. The chemistry of SFRMs tested is unknown but their generic types are readily identified from their physical appearance, and are listed in Table I. The substrates used were galvanized steel coupons with thicknesses of 0.35 mm and various widths: 6.35, 12.7, 19.05, 25.4, 38.1, and 50.8 mm. In addition, to study the influence of substrate type on the adhesion, structural steel coupons with thicknesses of 1.15 mm were also used to manufacture SFRM/steel specimens.

## 2.2. Specimen preparation and experimental setup

In field installation, the SFRM is typically applied to steel structures by spraying a SFRM slurry mixture through a spray nozzle onto steel structures. To simulate this field spray-applied action, we have devised a specimen preparation procedure which is outlined below (as shown in Figure 1) and fabricated at each respective manufacturer's location. Steel coupons with various widths were prepared having lengths of 230 mm. To facilitate attachment to the testing machine, 3.175 mm diameter holes were drilled in the steel substrates at a distance of 5 mm from each end. The substrates were then bent 90° at a distance of 10 mm from their respective ends (Figure 2). The substrates were rigorously cleaned using acetone. At the end of the substrate, where the load was to be applied, a thin layer of release agent was painted over a length of about 25 mm beginning at the bend and extending away from the hole to create a pre-crack. The joints were manufactured by constructing an open rectangular wood box consisting of a base panel with four side pieces. The dimension of the base panel was 635 mm × 300 mm × 19 mm. Two full length grooves were cut into the base panel to accommodate both the ends of the bent steel coupons. The grooves were 127 mm from centerline with a width of 6 mm, and a depth of 6.8 mm. The four side pieces had a height of 381 mm, which is equal to the thickness of the applied SFRM. These four sides were attached to the base panel using screws installed from the outside. The box was then lined with a release film to prevent the SFRM from adhering to the wood. The base panel was filled with substrates placed 15 mm apart with bent ends extending down into the grooves. The box was then shipped to a SFRM manufacturer where a SFRM was dispensed into the box in accordance with the manufacturer's recommendations until the box was completely filled. The whole assembly was then conditioned according to manufacturers' specification. Once the SFRM was cured, a support plate of thickness 5 mm was attached to the exposed SFRM surface using a commercial thermosetting adhesive. The completed boxes were then shipped back to the Building and Fire Research Laboratory at the National Institute of Standards and Technology. After allowing time for the adhesive between the support plate and the SFRM to fully cure, the wooden box was removed by flipping the assembly such that the support plate was on the bottom. Wooden base panel and sides were then carefully disassembled by removing screws holding the box together. The finished test joint is shown in Figure 2.

The end of each steel coupon was attached to a screw-driven testing machine and peeled away from the SFRM which was held fixed using a nominal cross-head displacement rate of 0.1 mm/s at 23 ± 2 °C. The load and displacement were measured continuously while a digital camera was used to monitor the propagation of debond or crack. No plastic deformation of the steel arms was observed in any of the tests. This is expected since, as will be shown later, the SFRM/steel interfacial and SFRM cohesive strengths are sufficiently weak so that the detaching force was not large enough to exceed the yield stress of the steel substrates. Three joints were tested for each

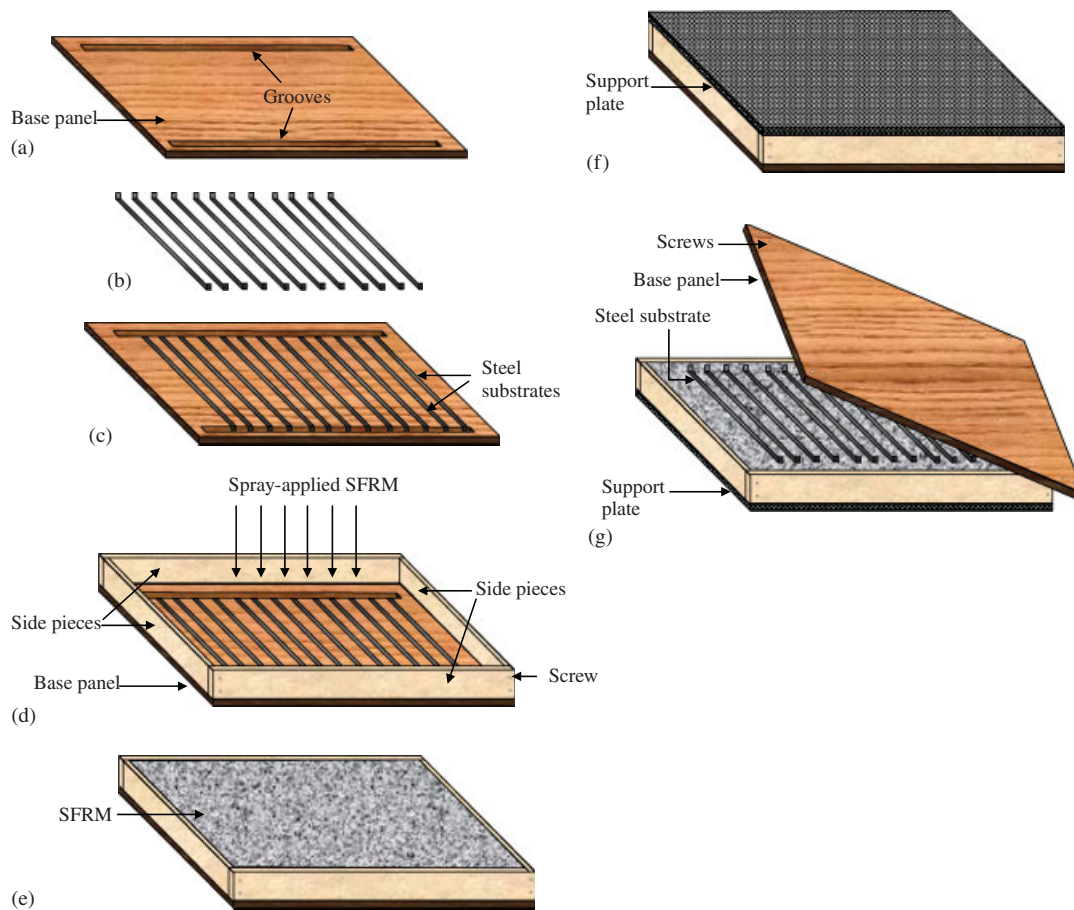


Figure 1. (a) Illustration of a base panel with two full length grooves, (b) steel substrates, (c) the base panel was filled with substrates placed 15 mm apart with bent ends extending into the grooves, (d) prior to dispensing a SFRM, four side pieces were attached to the base panel, (e) illustration of a SFRM filled box, (f) after the SFRM was cured, a support plate was attached to the exposed SFRM, and (g) the box was removed by flipping the assembly such that the support plate was on the bottom.

condition. Additionally, the morphology of galvanized and structural steels was analyzed using a Zeiss LSM510 laser scanning confocal microscope in the reflective mode with a laser wavelength of 543 nm. A series of optical z-scan slices each having a thickness of 100 nm were obtained. Three-dimensional images were digitally reconstituted from stacks of z-scan slices. Root-mean-square (RMS) surface roughness was calculated using a surface tilt correlation and an automatic plane algorithm [11].

### 2.3. Fracture mechanics analysis

In a typical setup shown in Figure 3, a substrate of thickness,  $h_s$ , and Young's modulus,  $E_s$ , is supported on a SFRM of thickness,  $h_a$ , and Young's modulus,  $E_a$ . The substrate is detached from the SFRM by loading one end of the substrate at a constant displacement rate while the other end was held fixed. The crack length,  $a$ , which is the distance between the loading end and the crack tip, is a measure of the adhesion strength of the interface. Assuming that the bonded joint exhibits bulk linear-elastic behavior, the value of fracture energy,  $G_C$ , may be deduced from the Griffith criterion of an energy balance [12]

$$G_C = \frac{P^2}{2b} \frac{dC}{da} \quad (1)$$

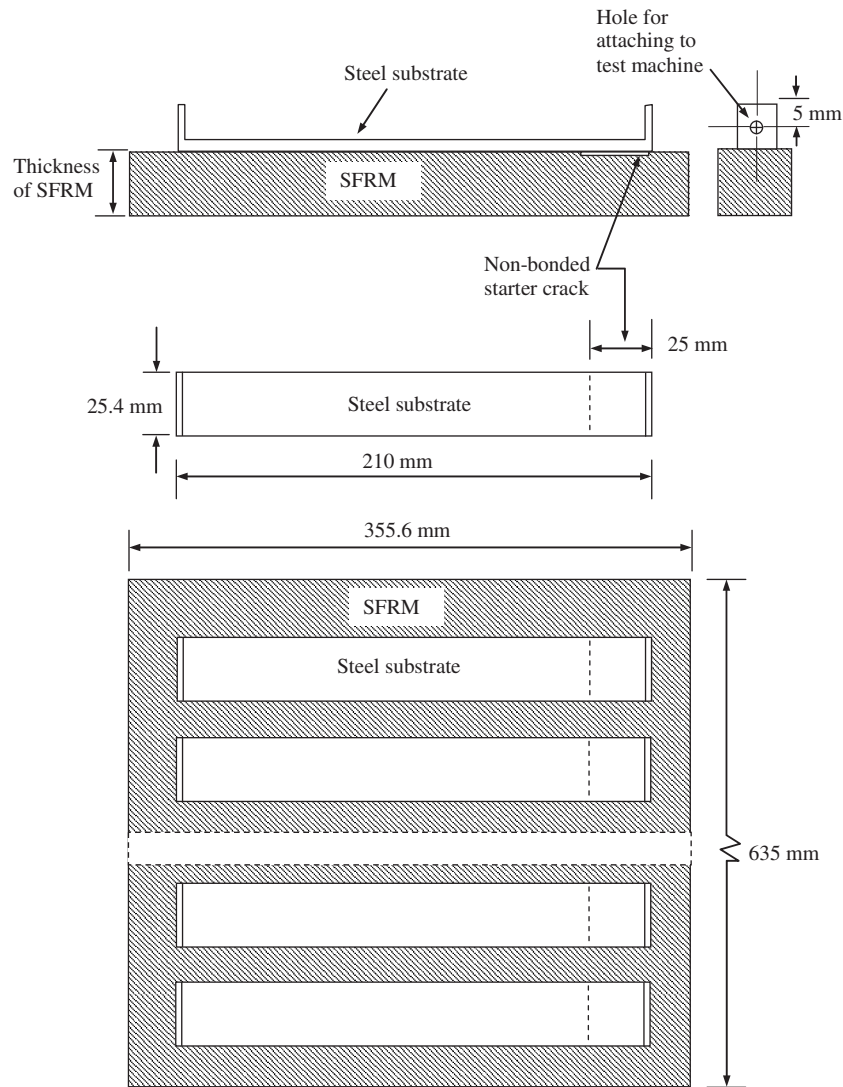


Figure 2. Schematic of single-arm cantilever beam test specimens (not to scale).

where  $P$  denotes the load at fracture,  $b$  the width of the substrate, and  $C$  the compliance (i.e.  $u/P$ , where  $u$  is the loading end displacement).

To determine  $u$ , we consider the SACB geometry as a beam on an elastic foundation [13–15] (see Figure 3(b)). The governing differential equation for  $u$  is given by

$$\begin{aligned} \frac{d^4 u}{dx^4} + 4\lambda^4 u &= 0 \quad \text{for } x \geq 0 \\ \frac{d^4 u}{dx^4} &= 0 \quad \text{for } x \leq 0 \end{aligned} \quad (2)$$

where

$$\lambda = \left( \frac{k}{4E_S I_S} \right)^{1/4} \quad (3)$$

and  $I_S$  is the bending moment of inertia of the substrate, and  $k$  is the stiffness of the foundation. The boundary conditions are that the shear force and the moment at the unloaded end ( $x = c$ ) are

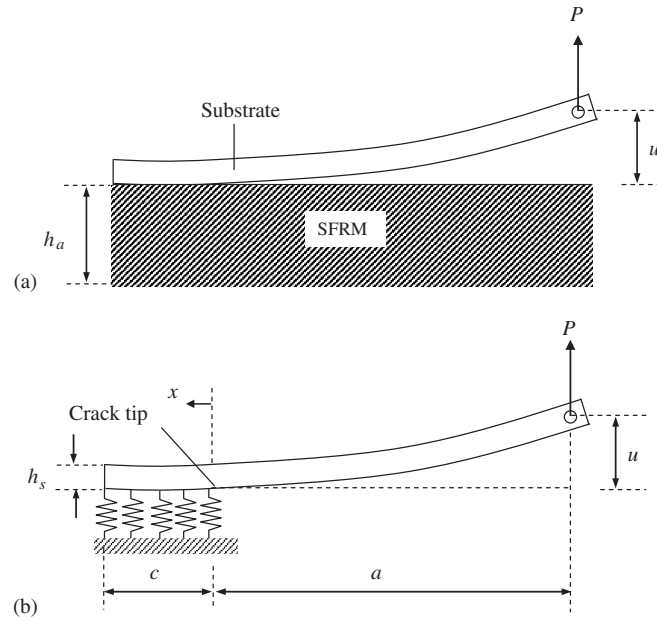


Figure 3. (a) Schematic of a single-arm cantilever beam and (b) a beam on an elastic foundation model (not to scale).

both zero, and those at the loading point ( $x = -a$ ) are equal to  $P$  and zero, respectively. Solving the two relationships in Equation (2) gives the following for  $u$  at  $x = -a$

$$u|_{x=-a} = \frac{12P}{E_S b h_S^3 \lambda^3} \left[ \frac{\lambda^3 a^3}{3} + \lambda a A + \lambda^2 a^2 B + \frac{1}{2} C \right] \quad (4)$$

where

$$A = \frac{\sinh^2 \lambda c + \sin^2 \lambda c}{\sinh^2 \lambda c - \sin^2 \lambda c}$$

$$B = \frac{\sinh \lambda c \cosh \lambda c + \sin \lambda c \cos \lambda c}{\sinh^2 \lambda c - \sin^2 \lambda c}$$

and

$$C = \frac{\sinh \lambda c \cosh \lambda c - \sin \lambda c \cos \lambda c}{\sinh^2 \lambda c - \sin^2 \lambda c} \quad (5)$$

The foundation stiffness,  $k$ , can be estimated from Hooke's law

$$k = \frac{E_a b}{h_a} \quad (6)$$

This expression is substituted in Equation (3), resulting in

$$\lambda = \left( \frac{3E_a}{E_S h_a h_S^3} \right)^{1/4} \quad (7)$$

A combination of Equations (1) and (4) gives the adhesive fracture energy as

$$G_C = \frac{6P^2(\lambda^2 a^2 + 2B\lambda a + A)}{E_S b^2 \lambda^2 h_S^3} \quad (8)$$

For a large value of  $c$  (i.e. crack propagation away from the unloaded end), hyperbolic terms are dominant in  $A$  and  $B$  of Equation (5), leading to  $A \rightarrow 1$ , and  $B \rightarrow 1$ . Thus, Equation (8) can be simplified to

$$G_C = \frac{6P^2(\lambda a + 1)^2}{E_S b^2 \lambda^2 h_S^3} \quad (9)$$

In this study,  $E_a$  used for the calculation of  $G_C$  was determined from quasistatic compression tests on free-standing SFRM blocks of dimension of  $40\text{ mm} \times 40\text{ mm} \times 40\text{ mm}$ . The values of  $E_a$  for SFRMs A through E are 2, 0.54, 11, 67, and 2.5 MPa, respectively. The vast range of moduli of SFRMs are results of different types and concentrations of fillers, binders, etc. in the SFRM formulations, allowing the exploration of a wide range of experimental regimes, from porous SFRMs to highly dense SFRMs.

An alternative approach to deduce  $G_C$  is to use an experimental compliance method (ECM) proposed by Berry [16], where  $C$  of the SACB can be expressed as a power-law compliance calibration of the form

$$C = C_0 a^n \quad (10)$$

where  $C_0$  and  $n$  are experimentally determined constants. Differentiating Equation (10) with respect to crack length and substituting in Equation (1) gives  $G_C$  as

$$G_C = \frac{n P u}{2 b a} \quad (11)$$

To determine  $G_C$  of the SFRM,  $n$  is first obtained as the slope in a least-squares fit in a log–log plot of  $C$  versus  $a$ . The values of  $P$ ,  $u$ , and  $a$  at fracture are then inserted into Equation (11). A difference between the analytical model (Equation (9)) and the ECM approach (Equation (11)) is the determination of  $dC/da$ , the compliance rate changes with respect to crack length. Note that Equation (9) involves  $a^2$  while Equation (11) involves  $1/a$ , which indicates that  $P$ ,  $u$ , and  $a$  are not independent variables. Thus, these variables must be considered when using the two data reduction methods as a means to test the  $G_C$  determination.

### 3. RESULTS AND DISCUSSION

#### 3.1. Crack resistance curve

For a wide range of specimen widths and SFRM types, stable crack growth was observed. While moving the cross-head, the load,  $P$ , and displacement,  $u$ , were recorded as a function of crack length,  $a$ . A typical plot of  $P$  versus  $u$  is shown in Figure 4. The curve is linear up to the maximum load followed by a decrease in  $P$  with  $u$ , indicating a stable crack growth behavior. The deviation from linearity and decrease in  $P$  indicate that the intensity of stress concentration ultimately reaches a critical level for crack propagation, which was confirmed by optical observations. After measuring the crack length, the specimen was immediately unloaded and the displacement returned to zero to ensure no plastic deformation occurring in the steel substrates. It was then reloaded to induce further crack extension and unloaded again. This procedure was repeated until catastrophic failure occurred. Although the steel bends to large deformation under load (Figure 4), when unloaded the steel returns to its planar, unbent configuration indicating no plastic deformation has occurred. Indeed, a small hysteresis was observed between different loading curves in Figure 4, confirming that our elastic treatment was valid.

By coupling these experiments with Equation (9), a crack resistance or R-curve is constructed by plotting  $G_C$  as a function of  $a$ . Figure 5 shows the results of a galvanized steel/SFRM B specimen with a substrate width of 6.35 mm. The value of  $G_C$  obtained from the initial crack length is the highest, which is attributed to the crack initiation from a blunt crack tip. The R-curve gradually decreases with increasing crack length as sharper crack tips develop, and eventually reaches a

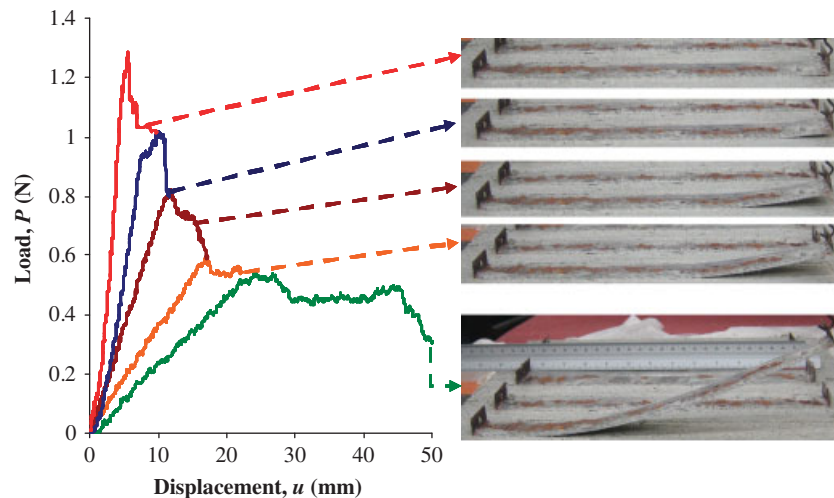


Figure 4. A typical load–displacement plot. Different curves represent a series of loading curves used to determine  $G_C$ . Typical crack velocity was 0.4 mm/s.

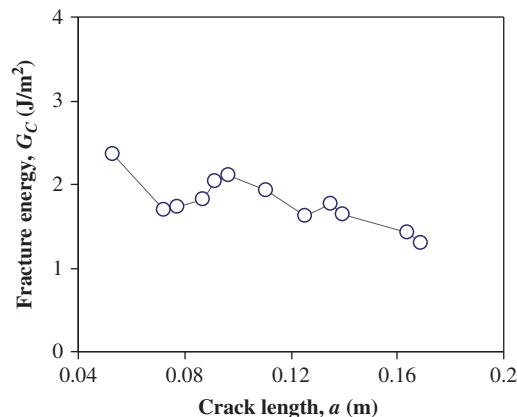


Figure 5. A typical fracture energy R-curve calculated using the beam on elastic foundation model. A line is added to aid the reader.

plateau with an approximate value of  $1.7 \text{ J/m}^2$ . The flattening R-curve observed here indicates that  $G_C$  is a constant during incremental crack advance, validating our fracture mechanics analysis for the specimen. Similar observations were made for all joints with various combinations of SFRM type and substrate width (not shown here for brevity). The results also show a very low value for  $G_C$  which indicates a brittle material where a linear elastic analysis should be valid and one might expect a flat R curve.

### 3.2. Comparison of the analytical model and ECM approach

The accuracy of the analytical model was verified by comparison with results from the ECM approach. If the analytical theory of the elastic foundation model is correct, the two data reduction methods of calculating  $G_C$  (i.e. Equations (9) and (11)) would necessarily give the same results. Figure 6 shows the typical log  $C$  versus log  $a$  curve in the ECM approach. A linear relation of the log–log plot allows  $n$  to be obtained, which is used in Equation (11) to calculate  $G_C$ . For a wide range of substrate widths and SFRMs, a good agreement was always observed between the analytical result in Equation (9) and the ECM approach. As an illustration, the results for the galvanized steel/SFRM C joints with a substrate width of 6.35 mm are listed in Table II.

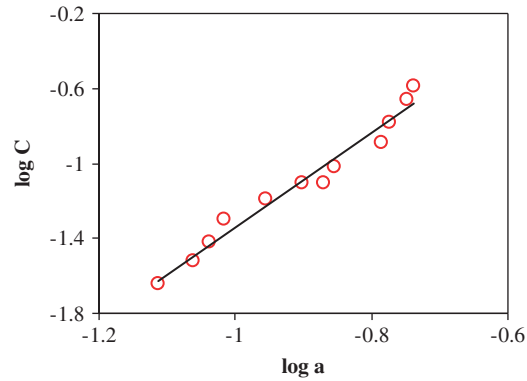


Figure 6. Log  $C$  versus log  $a$  plot. The straight line is the linear regression fit to the data with  $R^2=0.98$ .

Table II. Comparison between the values of  $G_C$  calculated from the analytical beam theory and the experimental compliance method for steel/SFRM 'C' joints with substrate width of 6.35 mm.

Data deduction method	Fracture energy $G_C$ (J/m <sup>2</sup> )
ECM	$5.69 \pm 0.51$
Analytical model	$5.75 \pm 0.84$

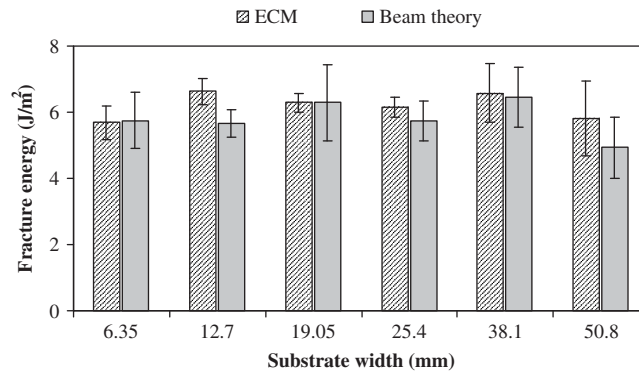


Figure 7. The values of  $G_C$  for SFRM C/steel joints with various substrate widths. Filled and hashed bars were calculated from the analytical model (Equation (9)) and the ECM approach (Equation (11)), respectively. The error bars represent a standard deviation from mean values.

Such an agreement between two different approaches indicates that the elastic foundation theory realistically simulates the SACB specimen geometry. Another point of interest in Figure 7 is that the scatter in the data as indicated by error bars was relatively small, signifying the reproducibility of the  $G_C$  values, which is of key importance in determining whether a test method is reliable.

### 3.3. Effect of substrate width

Figure 7 shows a comparison of the values of  $G_C$  calculated using Equations (9) and (11) for various substrate widths in joints of SFRM C supported on galvanized steel. It can be seen that the value of  $G_C$  is statistically independent of the substrate width. Similarly, results for the other four SFRMs show no effect of specimen width. This geometric independence suggests that fracture energy is a true material property for these systems. However, values of  $G_C$  for some materials, which are much tougher than SFRMs, have been shown to vary with substrate width [17]. The more

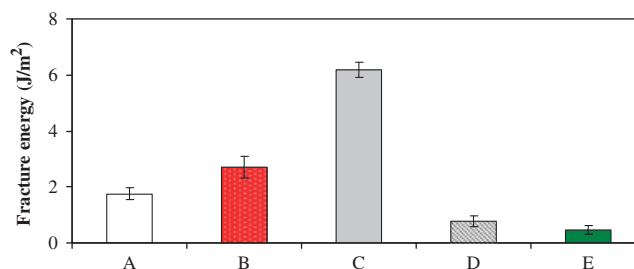


Figure 8. The fracture energy for various types of SFRM. The width of the substrate was 12.7 mm, and typical crack velocity was 0.4 mm/s. The error bars represent a standard deviation from mean values.

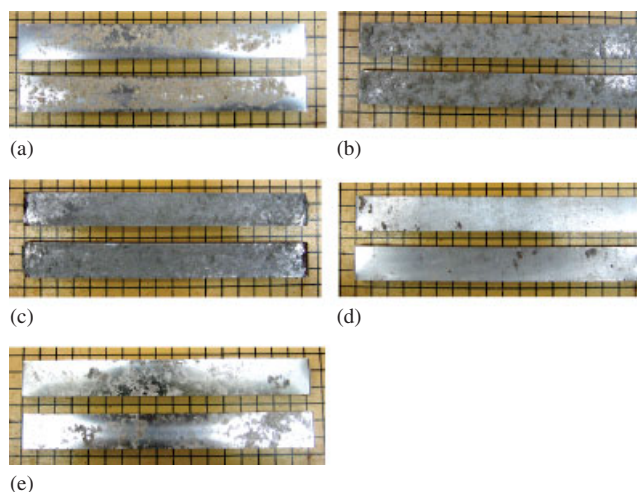


Figure 9. Optical images of fracture surfaces for SFRM (a) A, (b) B, (c) C, (d) D, and (e) E. The dimension of each square grid is 10 mm × 10 mm.

complex effect of substrate on  $G_C$  for these materials was ascribed to the influence of test geometry on the stress field around the crack tip leading to extensive plasticity and energy dissipation [17]. With the SFRMs, however, the behavior is brittle with a relatively weak interface so simple fracture mechanics should be applicable, and geometric independence can be expected. As a result, this test method provides an advantage over strength-based testing, and the  $G_C$  values obtained should be applicable to other geometries and useful for models that predict behavior and service life of bonded SFRM/steel structures.

### 3.4. Effect of SFRM types

The adhesion of SFRM systems consisting of a wide range of SFRM formulations were measured. Figures 8 and 9 show the values of  $G_C$  obtained for galvanized steel joints with a substrate width of 12.7 mm, and the corresponding optical microscopy images of fracture surfaces. Note that there are two potential weak links in a SFRM system, namely (a) the bulk SFRM itself, and (b) the interface between the substrate and SFRM. Failure occurs whenever the weakest link in this system fails. In this study, cohesive failure in the SFRM layer occurred in SFRMs B and C, indicating that a good interfacial adhesion was established across the substrate and the SFRMs, and it is the weak cohesive strength of the SFRMs that governed the ultimate failure of the systems. From Figure 8, we can see that the SFRM C has a higher intrinsic cohesive strength compared to SFRM B as indicated by its higher  $G_C$  value of 6.2 J/m<sup>2</sup>. Although the exact chemistry of the SFRMs was unknown, physical examinations revealed that SFRM B was a composite fireproofing product consisting of organic materials and inorganic fillers, whereas SFRM C was a cementitious product.

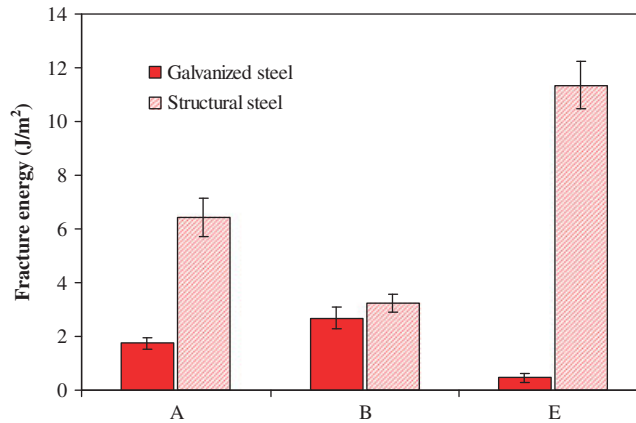


Figure 10. The dependence of  $G_C$  on the types of substrate. The error bars represent a standard deviation from mean values.

The possibility of a considerably large amount of inorganic fillers in SFRMs B behaving as defects in the joint cannot be precluded since failure could be easily initiated and propagated along these weak interfaces.

In contrast to SFRMs B through D, Figure 9 shows that SFRMs A and E failed via a complex path involving both cohesive and adhesive failures. Interfacial failure seems to be the dominant failure path in SFRM E. Despite the fact that both SFRMs are gypsum-based products having similar loci of failure, the value of  $G_C$  for SFRM E is relatively low compared to that of SFRM A (see Figure 8). This result clearly demonstrates the vastly different bulk strength of the SFRM within the same broad category, which is not surprising since there are various types and concentrations of fillers used in the formulations. In the case of SFRM D, its locus of failure differed from other SFRMs in that cohesive failure was predominant, but the SFRM retained on the failure surface was relatively thin, as shown in Figure 9(d). This fracture behavior suggests an interplay between the bulk cohesive strength and interfacial adhesion.

Figure 8, again, demonstrates the good reproducibility of the data as evidenced by the small error bars of three replicate experiments for each SFRM. Therefore, the SACB test method provides a quantitative and reproducible test method for measuring the adhesion of SFRM and steel. Efforts to use this new test method to examine the durability performance of SFRMs, including resistance to temperature extremes, moisture and vibration, are ongoing.

### 3.5. Effect of steel types

The values of  $G_C$  measured with structural steel are shown in Figure 10. As a point of comparison, data from the galvanized steel have been included on this figure. Note that the surface cleaning and the specimen width were kept the same for both steel types. With the exception of SFRM B, the values of  $G_C$  measured on structural steel generally exhibited better adhesion as compared to galvanized steel. This improved adhesion is particularly pronounced for SFRM E, where the fracture energy of the structural steel joint is 200 times greater than that of the galvanized steel joint. Optical examinations of the fracture surfaces revealed that the failure of structural steel joints occurred cohesively within the SFRMs, but with a higher portion of SFRMs retained on the surfaces of structural steel than that of galvanized steel. Therefore, a better adhesion is established across the SFRM and structural steel interface, which may be attributed to enhanced interfacial contact as a result of increased surface roughness in the structural steel. Indeed, laser scanning confocal microscopic measurements revealed that the RMS surface roughness of the structural steel is higher than that of the galvanized steel by a factor of two. Namely, the RMS surface roughness of galvanized steel for 5× and 150× are 3.208, and 0.239 μm, respectively; structural steel are 6.365, and 0.474 μm, respectively. The corresponding optical images are shown in Figure 11. The impact of substrate surface chemistry on adhesion performance, on the other hand, may be

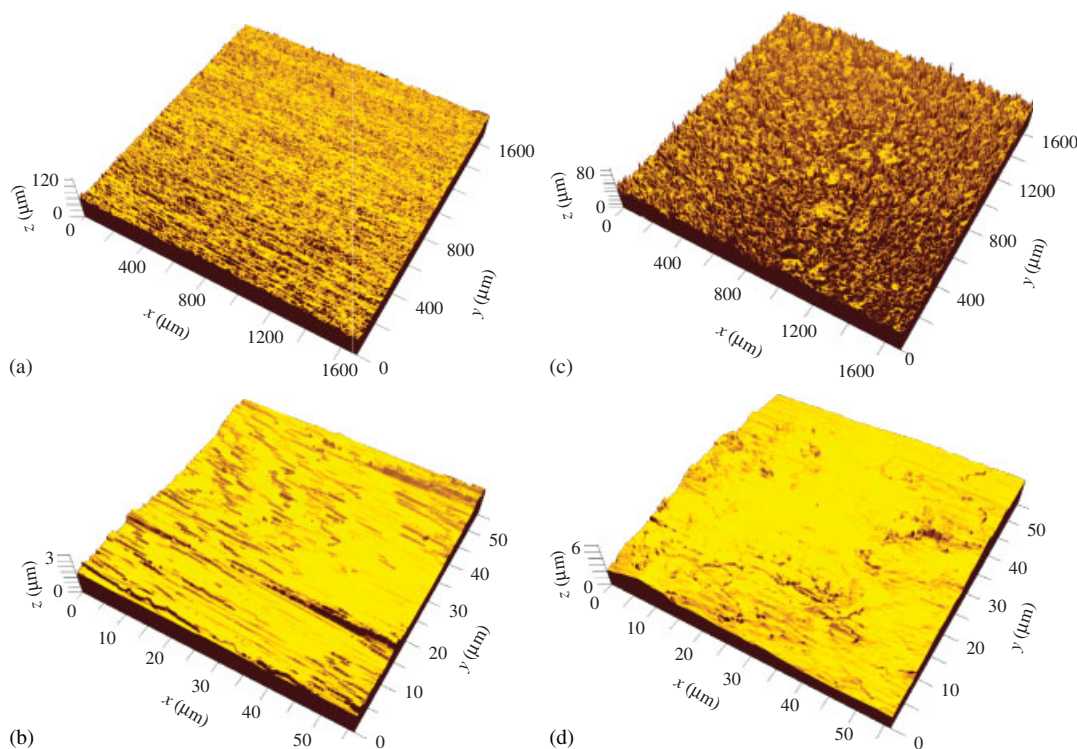


Figure 11. Laser scanning confocal microscopy images of galvanized steel substrate at magnifications (a)  $5\times$  and (b)  $150\times$ ; structural steel substrate at magnifications (c)  $5\times$  and (d)  $150\times$ .

minimal as indicated by relatively similar values of static contact angles of water for structural steel and galvanized steel. However, the variation in the amount of  $G_C$  increase for different SFRMs suggests that in addition to the interfacial interaction between the SFRM and steel, the bulk cohesive strength of SFRM plays an important role in the observed superior adhesion of SFRM with structural steel. Indeed, the physical basis of the measured  $G_C$  is the release of elastic energy in regions of the SFRM attached to the substrate as well as that from the detached portion of the SFRM.

### 3.6. Effect of test rate

The effect of test rate ranging from 0.005 to 0.5 mm/s on the measured values of  $G_C$  was examined for both galvanized and structural steels, which are shown in Figure 12. The test rates were selected to keep the duration of the experiment in a reasonable range. At the high rate (0.5 mm/s), a test takes about 1 min which allows adequate time to take the required pictures while the low rate (0.005 m/s) can be completed in under 1 h. In all the cases, the crack propagated in a stable, continuous manner. The values of  $G_C$  were found to be statistically independent of the test rate ranging over the three decades investigated here. The lack of rate dependence for the fracture behavior confirms that the failures were brittle with no or little viscoelastic dissipation. Therefore, the results, once again, reinforce that the measured  $G_C$  provides a unique failure criterion that is not a function of rate.

### 3.7. Comparison with the ASTM standard

The fracture mechanics approach described here measures the fracture energy or fracture toughness (resistance to failure via crack growth) of the SFRM/steel substrate interface or the SFRM itself depending on where the failure occurs. ASTM E736, on the other hand, measures strength,  $\sigma$ , which is a combination of toughness and the influence of the most critical flaw, void, defect, or

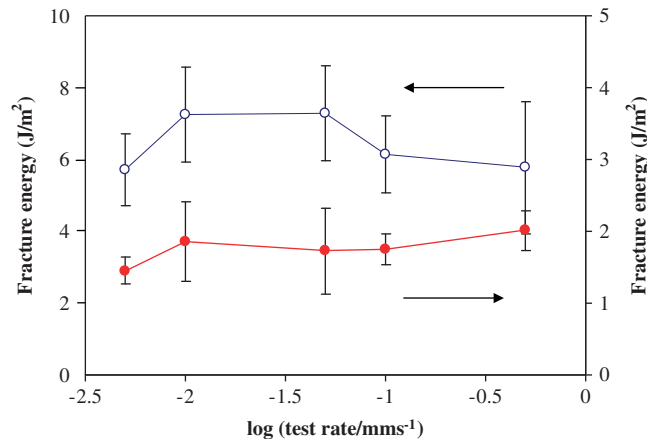


Figure 12. The dependence of  $G_C$  on test rate for galvanized steel (closed symbols) and structural steel (open symbols). The error bars represent a standard deviation from mean values.

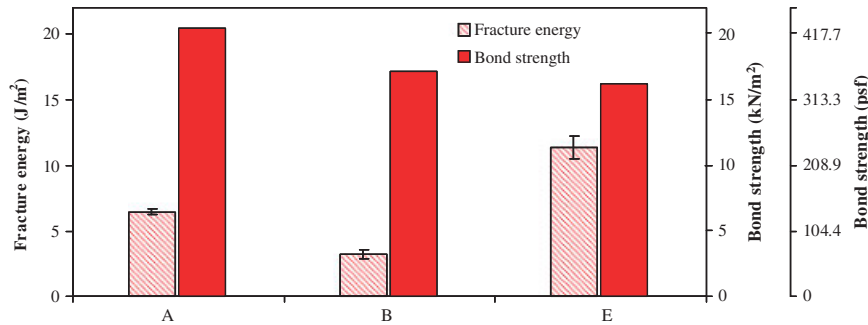


Figure 13. Comparison of results obtained from the SACB and ASTM E736 test methods. The error bars represent a standard deviation from mean values. Bond strength in pounds per square foot (psf) is added for reference.

debond introduced during fabrication

$$\sigma = \frac{P}{A} \quad (12)$$

where  $P$  is the applied force and  $A$  is the bonded area of the metal or plastic disk. As a result, it is not possible to quantitatively compare the two tests without knowledge about the most critical flaw, etc. Nonetheless, bond strength values for structural steel measured in accordance with the ASTM E736 for three SFRMs (obtained from the manufacturers) and the fracture energy values measured from the new test method can be compared in terms of relative values and rank order, which is shown in Figure 13. Distinct rank orders are obtained from both the test methods. The fracture mechanics approach shows that, among all the three SFRMs, SFRM E produced the highest fracture energy with structural steel. However, according to the ASTM standard test method, the strength between SFRM A and structural steel is superior to that of the SFRMs B and E. Also, while the ASTM test method gives both SFRMs B and E an equivalent strength rating, the fracture mechanics approach indicates that SFRM E outperforms SFRM B with its value of  $G_C$  approximately 250% greater than that of SFRM B.

To further compare the ASTM standard tests and fracture mechanics approach, note first that cohesive failures within the SFRM layers were always observed for structural steel substrates.

Thus, the fracture energy,  $G_C$ , can be correlated to the stress intensity factor,  $K_C$ , as [18]

$$G_C = \frac{K_C^2}{E'} \quad (13)$$

where  $E' = E_a$  for plane stress,  $E' = E_a/(1 - \nu_a^2)$  for plane strain with  $E_a$  and  $\nu_a$  are Young's modulus and Poisson's ratio of the SFRM, respectively. The solution for stress intensity factor in any plane elasticity problem for an arbitrary crack of size  $a$  will have the form

$$K_C = Y\sigma\sqrt{\pi a} \quad (14)$$

where  $Y$  is the geometry factor and  $\sigma$  is the applied stress. Equations (13) and (14) can then be combined to give the relationship between  $\sigma$  and crack length (flaw size)

$$\sigma = \frac{1}{Y} \sqrt{\frac{E' G_C}{\pi a}} \quad (15)$$

Thus, an advantage of fracture energy is that one can predict what strength value would be obtained for any given flaw, void, defect, or debond, and *vice versa*. Consider SFRMs A and E, the ASTM standard test gives SFRM A the highest strength while the fracture mechanics test indicates SFRM E has the highest  $G_C$  value. Equation (15) shows that maximum flaw size which can be tolerated without failure under an applied  $\sigma$  in the SFRM E is twice the size of that for SFRM A. Thus, this simple argument clearly shows the deleterious effect of defects on adhesion of SFRM A since both SFRMs have approximately the same values of  $E_a$ . Given that the modulus ratio SFRM E to SFRM B is 4.6 (see Section 2.3), the critical value of  $a$  for crack propagation under a given  $\sigma$  in SFRM B is 18 times lower the value for SFRM E. This is a result of the very low fracture resistance of SFRM B. Consequently, to achieve the same ultimate tensile strength in both SFRMs B and E, the former must be fabricated with much smaller flaws.

As mentioned earlier, the interpretation of ultimate tensile strength has its limitation, i.e. specimens typically fail at some unknown local critical stress state. The ultimate stress values represent the average stress state on the whole sample whereas joint rupture is generally a local phenomenon initiated at pre-existing defects. Unless the nature and magnitude of the stresses are known, quantitative prediction of adhesion failure is not possible. A test method with a predictive capability for adhesion integrity and reliability is highly sought after because it minimizes the need for expensive and time-consuming testing. Furthermore, the strength-based approach ignores the fact that defects such as surface roughness, contaminants, cracks, pits, etc., are inevitably present in the real world structures and these features significantly weaken adhesion. The failure criterion derived from the fracture mechanics approach corrects for these shortcomings by capturing all the energy losses occurring around the crack tip with a rigorous theoretical analysis. Instead of solely relying on applied stresses as in the strength-based approach, fracture mechanics provides a more realistic method for quantifying adhesion for vast majority of situations where failure occurs by crack initiation and propagation from a stress concentration point. Currently, there is a serious lack of guidance for evaluating the performance of SFRMs. This new test method will be a valuable tool for defining adhesion performance requirements, and evaluating adhesion performance.

#### 4. CONCLUSIONS

A new test method for measuring adhesion between SFRMs and steel structures using a fracture mechanics approach has been presented. In this test method, an energy-based criterion for fracture was adopted, which measures the fracture energy,  $G_C$ , required to detach a SFRM from a steel structure. Two independent approaches were utilized to calculate  $G_C$ , an analytical beam theory and an experimental compliance calibration method. Good agreement in the values of  $G_C$  from these two approaches was obtained, validating the theoretical and experimental basis for this approach. Various combinations of SFRM formulations, steel types, substrate width and test rate, were examined using this new test method. It was evident that this test method provides a robust

methodology for quantitatively evaluating the adhesion between SFRMs and steel structures. This test method should contribute to an improved quantification of adhesion requirements for fire protection design.

#### ACKNOWLEDGEMENTS

The authors thank Dale Bentz, Joannie Chin, Jon Martin, and Fahim Sadek of NIST for their helpful discussions; Yongyan Pang and Lipiin Sung of NIST for surface roughness measurements. Financial and technical support of the members of the Performance Assessment and Optimization of Fire Resistant Materials Consortium are greatly appreciated.

#### REFERENCES

1. Fire protection of structural steel in high-rise buildings. Goode MG (ed.). NIST GCR 04-872, 2004.
2. Report on steel column protected by metal lath and vermiculite plaster, Underwriters' Laboratories, Inc., pp. 22, January 7, 1947.
3. Proceedings of fire resistance determination and performance prediction research needs workshop. Grosshandler WL (ed.). NISTIR 6890, 2002.
4. Gewain RG, Iwankiw NR, Alfawakhiri F. Facts for Steel Building—Fire. American Institute of Steel Construction, Inc., 2003.
5. Lieff M. Fire resistant coverings, fire resistive coatings: the need for standards. In *ASTM STP 826*, Lieff M, Stumpf FM (eds). American Society for Testing and Materials, 1983; 3–13.
6. Bentz DP, White CC, Prasad KR, Flynn DR, Hunston DL, Tan KT. A materials science-based approach to characterizing fire resistive materials. *Journal of ASTM International* 2009; **6**(5).
7. ASTM E736. Standard test method for cohesion/adhesion of spray fire-resistive materials applied to structural members. *Annual Book of ASTM Standards*, vol. 04.11. ASTM International: West Conshohocken, 2006.
8. Federal building and fire safety investigation of the World Trade Center disaster. *Final Report on the Collapse of the World Trade Center*, NIST NCSTAR 1, U.S. Department of Commerce, September 2005.
9. Zanghi PA. Post impact—the focus on durability of fire-resistive materials in structures. *NFPA Journal* 2005; **99**(5):80–85.
10. World Trade Center building performance study—data collection, preliminary observation and recommendations, FEMA 403, May 2002.
11. Faucheu J, Sung L, Martin JW, Wood KA. *JCT Research* 2006; **3**:29–39.
12. Griffith AA. The phenomena of rupture and flow in solids. *Philosophical Transactions of the Royal Society London A* 1920; **221**:163–198.
13. Kanninen MF. Augmented double cantilever beam model for studying crack propagation and arrest. *International Journal of Fracture* 1973; **9**:83–92.
14. Williams JG. Fracture in adhesive joints—the beam on elastic foundation model. *Proceedings of ASME International Mechanical Engineering Congress and Expositions*, San Francisco, California, 1995; 1112–1117.
15. Kanninen MF. Dynamic analysis of unstable crack propagation and arrest in the DCB test specimen. *International Journal of Fracture* 1974; **19**:415–430.
16. Berry JP. Determination of fracture surface energies by the cleavage technique. *Journal of Applied Physics* 1963; **34**:62–68.
17. Kinloch AJ, Shaw SJ. The fracture-resistance of a toughened epoxy adhesive. *Journal of Adhesion* 1981; **12**:59–77.
18. Wang SS, Mandell JF, McGarry FJ. An analysis of the crack tip stress field in DCB adhesive fracture specimens. *International Journal of Fracture* 1978; **14**:39–58.